Modeling the transport of aggregating nanoparticles in porous media

by

Vasileios E. Katzourakis* and Constantinos V. Chrysikopoulos

School of Environmental Engineering, Technical University of Crete, Chania 73100, Greece

Manuscript to be submitted to
Water Resources Research

Key words: nanoparticles, transport, aggregation, reversible attachment, irreversible attachment, porous media, mathematical modeling.

November 8, 2020

*Corresponding author (biliskatz@yahoo.gr).

Abstract

A novel mathematical model was developed to describe the transport of nanoparticles in water saturated, homogeneous porous media with uniform flow. The model accounts for the simultaneous migration and aggregation of nanoparticles. The nanoparticles are assumed to be found suspended in the aqueous phase or attached reversibly or irreversibly onto the solid matrix. The Derjaguin-Landau-Verwey-Overbeek theory was used to account for possible repulsive interactions between aggregates. Nanoparticle aggregation was represented by the Smoluchowski population balance equation (PBE). Both reaction-limited aggregation and diffusion-limited aggregation were considered. Particle-size dependent dispersivity was accounted for. In order to overcome the substantial difficulties introduced by the PBE, the governing coupled partial differential equations were solved by employing adaptive operator splitting methods, which decoupled the reactive transport and aggregation into distinct physical processes. The results from various model simulations showed that the transport of nanoparticles in porous media is substantially different than the transport of conventional biocolloids. In particular, aggregation was shown to either decrease or increase nanoparticle attachment onto the solid matrix, depending on particle size, and to yield early or late breakthrough, respectively. Finally, useful conclusions were drawn regarding possible erroneous results generated when aggregation, particle-size dependent dispersivity or nanoparticle surface charges are neglected.

1. Introduction

In recent years, nanotechnology has become one of the most promising industry sector with many applications in healthcare, medicine, molecular biology, semiconductor physics, and agriculture. However, despite their significant benefits some nanomaterials, such as metal oxide nanoparticles are considered toxic (IARC, 2010). Nanoparticles enter the environment from wastewaters originating from industrial or house-hold sources, which do not undergo proper treatment (Benn & Westerhoff, 2008; Brar et al., 2010; Gottschalk et al., 2009; Mueller & Nowack, 2008), and from accidental release or inappropriate disposal of nanomaterials (Brar et al., 2010; Nowack &

Bucheli, 2007; Wiesner et al., 2006). These nanomaterials often contribute to the pollution of aquatic and other terrestrial environments.

Nanoparticle transport differs significantly from conventional biocolloid transport, because particles may aggregate and form larger particles with different physical characteristics (Solovitch et al., 2010). Consequently, the classical filtration theory may fail to capture the attachment dynamics of nanoparticles (Chen et al., 2011; Chowdhury et al., 2011; Fang et al., 2009; Godinez & Darnault, 2011; Heidmann, 2013; Zhang et al., 2014). The aggregation process can be classified into two distinct categories: (i) diffusion-limited aggregation (DLA), and (ii) reaction-limited aggregation (RLA) (Wijnen et al., 1991; Gaudreault et al., 2015). When no repulsive forces are present between particles, then every collision leads to attachment. This is essentially a DLA process, which is usually referred to as “fast aggregation” and yields aggregates with plenty of void spaces. If repulsive forces exist between particles, then aggregation is slowed down because multiple collisions may be needed before a successful particle attachment. This is a RLA process, which is usually referred to as “slow aggregation” and produces dense aggregates (Gaudreault et al., 2015; Lin et al., 1990; Weitz et al., 1991; Weitz & Lin, 1986).

Nanoparticle aggregation is an important process for particle attachment during transport in porous media. However, the available mathematical models for particle transport, which are based on colloid filtration theory (CFT), depth-dependent retention and blocking, despite their success in fitting relatively well experimental data, frequently do not capture the physicochemical processes that nanoparticles undergo during transport in porous media (Goldberg et al., 2014). Also, the available mathematical models that try to couple the transport equation with an expression for aggregation (Chatterjee & Gupta, 2009; Raychoudhury et al., 2012; Taghavy et al., 2015; Quik et al., 2015; Babakhani et al., 2018) may provide improved results, but either they do not take into account for appropriate particle dispersion or they fail to account for the existence of repulsive forces between charged particles. Other models use simplifying or empirical reaction rates (Babakhani et al., 2019), and general attachment equations (Wang et al, 2018) to account for transport and aggregation of particles. The mathemtical model developed by Babakhani (2019) takes into account transport and aggregation of nanoparticles and evaluates their size exclusion. It was shown that accounting for particle aggregation improved substantially the predictive ability of the model. However, the Babakhani (2019) mathematical model does not contain explicit transport and aggregation terms and does not account for thorough particle attachment onto the solid matrix (e.g. with a two site reversible/irreversible kinetic model).

The aim of this work is to develop a novel mathematical model for the description of the transport of aggregating nanoparticles, in water saturated, homogeneous porous media, with fully developed uniform flow, in which there is a clear formulation of how transport and aggregation terms are coupled. The model accounts for changes in particle attachment onto the solid matrix due to evolving size of aggregated particles and for potential repulsive interactions between particles. To the best of our knowledge such unique model for the transport of suspended nanoparticles undergoing two-site attachment and aggregation in porous media is not available in literature.

2. Mathematical developments

2.1 Transport of nanoparticles

The proposed nanoparticle transport model assumes that particles can aggregate and partition between the aqueous phase and the solid matrix. The forming aggregates can be classified based on their average diameter into k clusters, where k=1,2,3... is the cluster incremental number (i.e. cluster $k=1$ consists of monomers, while cluster $k=2$ consists of dimers). Nanoparticles can be found suspended in the aqueous phase with number concentration n_k [np_k/L^3] (where np_k is the number of aggregates of cluster k), or attached onto the solid matrix n_k^* [np_k/M_s] (where M_s is the mass of the solid matrix). Consequently, the governing partial differential equation describing the transport of nanoparticles that belong to cluster k, in one-dimensional, homogeneous, water saturated porous media with developed one-directional uniform flow, accounting for non-equilibrium attachment onto the solid matrix is essentially the well-established transport equation for colloids (Sim & Chrysikopoulos, 1998; Katzourakis & Chrysikopoulos, 2014) written in terms of particle number density (number concentration instead of mass concentration) with an additional sink/sourse term which accounts for nanoparticle aggregation (Lee et al., 2000; Sabelfeld & Kolodko, 2002):

$$\frac{\partial n_k(t,x)}{\partial t}+\frac{\rho_b}{\theta}\frac{\partial n_k^*(t,x)}{\partial t}-\left(D_x\right)_k\frac{\partial^2 n_k(t,x)}{\partial x^2}+U\frac{\partial n_k(t,x)}{\partial x}=\left(F_n\right)_k(t,x)+\left(A_n\right)_k(t,x) \qquad (1)$$

where U [L/t] is the average interstitial velocity; $\left(D_x\right)_k$ [L^2/t] is the longitudinal hydrodynamic dispersion coefficient of the suspended nanoparticles that belong to cluster k; ρ_b [M_s/L^3] is the bulk density of the solid matrix; θ [-] is the porosity of the porous medium; x [L] is the spatial coordinate in the longitudinal direction; t [t] is time; $\left(F_n\right)_k(t,x)$ [np_k/L^3t] is a general source configuration form of the nanoparticles that belong to cluster k; and $\left(A_n\right)_k(t,x)$ [np_k/L^3t] is the aggregation source/sink term for nanoparticles that belong to cluster k.

The nanoparticle aggregation source/sink term is assumed to be accurately represented by the Smoluchowski population balance equation (PBE), which describes the evolution of the mass spectrum of a collection of particles due to successive merges (Smoluchowski, 1916):

$$\left(A_n\right)_k=\frac{dn_k}{dt}=\frac{1}{2}\sum_{i=1}^{k-1}b_{i,k-i}n_i n_{k-i}-n_k\sum_{i=1}^{\infty}b_{k,i}n_i \qquad (2)$$

where $b_{i,k}$ is an aggregation kernel, referring to the collision frequency of the nanoparticles. The 1/2 multiplier in front of the first summation term corrects for the double counting of particle collisions.

The attachment of nanoparticles onto the solid matrix is assumed to be reversible or irreversible. Consequently, the number density of nanoparticles attached onto the solid matrix, n_k^* [np_k/M_s], is the sum of the reversibly, $n_k^{*(r)}$ [np_k/M_s], and irreversibly, $n_k^{*(i)}$ [np_k/M_s], attached particle concentrations:

$$n_k^*=n_k^{*(r)}+n_k^{*(i)} \qquad (3)$$

Therefore, the corresponding nanoparticles accumulation term in equation (1) is expressed as:

$$\frac{\partial n_k^*}{\partial t}=\frac{\partial n_k^{*(r)}}{\partial t}+\frac{\partial n_k^{*(i)}}{\partial t} \qquad (4)$$

The reversible nanoparticle accumulation term is described by the following nonequilibrium equation (Sim & Chrysikopoulos, 1998; Sim & Chrysikopoulos, 1999):

$$\frac{\rho_b}{\theta}\frac{\partial n_k^{*(r)}}{\partial t} = r_{n_k - n_k^{*(r)}} n_k - r_{n_k^{*(r)} - n_k}\frac{\rho_b}{\theta} n_k^{*(r)} \qquad (5)$$

where $r_{n_k - n_k^{*(r)}}$ [1/t] is the rate coefficient of reversible nanoparticle attachment onto the solid matrix, and $r_{n_k^{*(r)} - n_k}$ [1/t] is the rate coefficient of reversible nanoparticle detachment from the solid matrix. The irreversible accumulation term is described by the following nonequilibrium equation (Compère et al., 2001; Katzourakis & Chrysikopoulos, 2014):

$$\frac{\rho_b}{\theta}\frac{\partial n_k^{*(i)}}{\partial t} = r_{n_k - n_k^{*(i)}} n_k \qquad (6)$$

where $r_{n_k - n_k^{*(i)}}$ [1/t] is the rate coefficient of irreversible nanoparticle attachment onto the solid matrix. It should be noted that under steep velocity changes or time varying salinity and pH fluctuations alternative expressions to equation (5) exist in the literature (Bedrikovetsky et al., 2011, 2012; Russell & Bedrikovetsky, 2018).

The general form of the source configuration of the nanoparticles of cluster k, can be written as (Sim & Chrysikopoulos, 1999):

$$\left(F_n\right)_k(t,x) = G_k(t)\, W(x) \qquad (7)$$

where $G_k(t)$ [np_k/L^2t] is the particle release function, and W(x) [1/L] describes a point source geometry:

$$W(x) = \delta(x\text{-}x_0) \qquad (8)$$

where $\delta(x\text{-}x_0)$ [1/L] is the Dirac delta function, and x_0 [L] is the Cartesian x-coordinate of the source centre. For a broad pulse, the function $G_k(t)$ is given by:

$$G_k(t) = \frac{Nr_k}{\theta} H(t_p - t) \qquad (9)$$

where Nr_k [np_k/L^2t] is the point source release rate of particles that belong to cluster k; t_p [t] is the source release period over which nanoparticles enter the porous medium; and H(t) [–] is the unit step or Heaviside function ($H(t<0)=0$, $H(t\geq 0)=1$). For an instantaneous source, $G_k(t)$ is given by:

$$G_k(t)=\frac{\left(N_{inj}\right)_k}{A_c\theta}\delta(t) \tag{10}$$

where $\left(N_{inj}\right)_k$ [np_k] is the injected number of particles that belong to cluster k, A_c [L^2] is the cross-sectional area of the porous medium, and $\delta(t)$ [1/t] is the Dirac delta function. Note that using equations (7)-(10), it is possible to define a broad pulse or instantaneous nanoparticle point source, located anywhere within the aquifer with x-coordinate $x=x_0$.

2.2 Initial and boundary equations

The initial condition and the appropriate boundary conditions for a one-dimensional confined aquifer with finite dimensions are as follows:

$$n_k(0,x)=0 \tag{11}$$

$$n_k(t,0)=\begin{cases} n_k^0, & t\leq t_p \\ 0, & t>t_p \end{cases} \tag{12}$$

$$n_k(t,0)=0 \tag{13}$$

$$\frac{\partial n_k^2(t,\, L_x)}{dx^2}=0 \tag{14}$$

where L_x [L] is the length of the porous medium and n_k^0 [np_k] is the initial constant aqueous phase concentration of cluster k. Condition (11) establishes that initially there are no nanoparticles within the porous medium. Condition (12) represents a broad pulse injection with constant nanoparticle concentration at the inlet. Condition (13) indicates that nanoparticles are not entering the aquifer through the inlet, but they are injected at a specific location within the aquifer according to equations (7)-(10). The downstream boundary condition (14) preserves concentration slope continuity for the finite length aquifer (Shamir & Harleman, 1967). It should be noted that the initial and boundary conditions (11)-(14) are applied k times, once for each cluster.

2.3 Aggregation kernel

The term $b_{i,j}$ in equation (2) represents the collision rate between particles that belong to clusters i and j. A variety of collision frequency kernels are available in the literature that account for different physicochemical conditions. One of the most commonly used kernels for DLA processes (Axford, 1997; Smoluchowski, 1917), which accounts for collisions resulting from Brownian diffusion while ignoring negligible contributions from fluid shear and sedimentation (Petosa et al., 2010; Taghavy et al., 2015) is:

$$b_{ij}^{DLA} = \frac{2k_B T}{3\mu_w} \frac{(r_i + r_j)^2}{r_i r_j} \tag{15}$$

where k_B [$M \cdot L^2/(t^2 \cdot T)$] is the Boltzmann constant; T [K] is temperature; r_k [L] is the radius of a nanoparticle that belongs to cluster k; and μ_w [M/(t·L)] is the dynamic viscosity of water. The ratio $k_B T/\mu_w$ characterizes the diffusion of suspended particles due to Brownian movement. Larger values of this ratio (caused by temperature increase) result to increased collision frequency. Also, the parabolic ratio $(r_i+r_j)^2/r_i r_j$ indicates that the collision frequency is higher between particles of different sizes than for particles of the same size. For RLA processes, the collision frequency kernel, b_{ij}^{RLA}, must account for repulsive forces produced when similarly charged particles interact. This can be achieved by using the Fuchs stability ratio $w_{ij} > 1$ [-], which is defined as the ratio of aggregation rate of a particle in the absence of repulsive interactions to the aggregation rate when the repulsive interactions are present (Fuchs, 1934; Lattuada et al., 2003). Values of w_{ij} close to unity indicate fast aggregation and refer to an "unstable" particle suspension, while larger values of $w_{ij} >> 1$ indicate slow aggregation and refer to a "stable" particle suspension. The b_{ij}^{RLA} is related to b_{ij}^{DLA} as follows (Amal et al., 1990; Arosio et al., 2012):

$$b_{ij}^{RLA} = \frac{b_{ij}^{DLA}}{w_{ij}} \tag{16}$$

where w_{ij} [-] can be expressed as (Axford, 1997; Liu et al., 2011; Reerink & Overbeek, 1954):

$$w_{ij}=2\int_{2}^{\infty}\exp\left[\frac{(\Phi_{tot})_{ij}}{k_B T}\right]\frac{1}{s^2}ds \quad (17)$$

where the dimensionless parameter s [-] is given by:

$$s=\frac{2R}{r_i+r_j} \quad (18)$$

where R [L] is the distance between the centers of two colliding particles; r_i [L] and r_j [L] are the radii of particles i and j, respectively; $(\Phi_{tot})_{ij}$ [M·L^2/t^2] is the total interaction energy between particles i and j, which is a function of s and can be calculated from the DLVO theory. It is evident from equation (17) that the ratio of the interaction energy to the thermal energy $(\Phi_{tot})_{ij}/k_BT$ dictates the value of stability ratio w_{ij}. If the available energy k_BT is consistently greater than the energy barrier $k_BT > (\Phi_{tot})_{ij}$, regardless of distance s, then the Fuchs ratio will obtain values close to unity $w_{ij} \approx 1$ and fast aggregation DLA will occur. Otherwise, the existing thermal energy k_BT will not be able to overcome easily the energy barrier and slow aggregation RLA will take place. Furthermore, the dimensionless distance of the two particles, s, indicates that the effects of the energy barrier $(\Phi_{tot})_{ij}$ decay fast with distance. Therefore, increased interaction potential over shorter distances leads to higher Fuchs stability ratio w_{ij}.

2.4 Aggregate structure

According to the coalesced sphere assumption, two spherical particles collide and form a new spherical aggregate. The mass of the produced aggregate is the sum of the masses of the two initial particles, while the same is true for their volumes. Therefore, the aggregate density is maintained constant. However, in reality, the resulting aggregates contain void spaces. The relation between the diameter of the final aggregate, $(d_p)_k$, and the initial monomer, $(d_p)_1$, is (Feder, 1988; Lee et al., 2000):

$$(N_P)_k=\zeta\left[\frac{(d_P)_k}{(d_P)_1}\right]^{D_F} \quad (19)$$

where $\left(N_P\right)_k$ [np$_k$] is the number of particles present in an aggregate that belongs to cluster k; $\left(d_p\right)_k$ [L] is the diameter of the produced aggregate that belongs to cluster k; ζ [-] is the packing factor, which accounts for the void pore space within the spherical aggregate and depends on the shape of both monomers and aggregates; D_F [-] is the fractal dimension of an aggregate and depends on the type of aggregation. For spherical monomers in close packing ζ=0.7405, whereas, in random packing ζ=0.637 (Feder, 1988). The slow RLA process usually yields aggregates with D_F=2.1, while the fast DLA yields aggregates with D_F=1.75 (Gaudreault et al., 2015; Lin et al., 1989). Finally, the mean particle diameter of aggregates suspended in the solution, $\overline{d}_P$ [L], can be written as a function of the individual aggregate diameters:

$$\overline{d}_P = \frac{\sum_{i=1}^{k} \left(N_P\right)_i \left(d_P\right)_i}{\sum_{i=1}^{k} \left(N_P\right)_i} \tag{20}$$

Equations (16) and (17) for the description of aggregation kernel b_{ij}^{RLA} are not practical, because the exact way that the total interaction potential $\left(\Phi_{tot}\right)_{ij}$ scales with the aggregate size, frequently is unknown. Therefore, in the absence of experimental information relating the aggregate structure, a scaling factor P_{ij} is used (Arosio et al., 2012; Nicoud et al., 2014; Sandkühler et al., 2004) and equation (16) takes the form:

$$b_{ij}^{RLA} = \frac{b_{ij}^{DLA}}{w_{11}} P_{ij} \tag{21}$$

where w_{11} [-] is the Fuchs ratio for aggregation of two monomers; P_{ij} [-] is often represented by the product kernel: $P_{ij}=(ij)^{\lambda}$ (Arosio et al., 2012; Family et al., 1985), which has been proven to perform well (Lattuada et al., 2003; Nicoud et al., 2014). The value of the exponent λ [-] is typically within the range 0.25-0.5 (Lin et al., 1990; Sandkühler et al., 2004). Assuming that the interactions between two aggregates are governed mainly by the monomers on the surface of the aggregates, the coefficient λ can be expressed analytically as $\lambda = 1 - 1/D_F$ (Arosio et al., 2012; Nicoud et al., 2014), and b_{ij}^{RLA} becomes:

$$b_{ij}^{RLA} = \frac{b_{ij}^{DLA}}{W_{11}} (ij)^{1-\frac{1}{D_F}} \tag{22}$$

Note that b_{ij}^{RLA} should never be greater than b_{ij}^{DLA}, because the latter one is the maximum aggregation rate, where every collision results in aggregation. Consequently, if the ratio W_{11} / P_{ij} <1, it must be set equal to unity (Sandkühler et al., 2004). Please note that DLA occurs in the absence of repulsive interactions, making aggregates with lower fractal dimensions, while RLA occurs in the presence of repulsive interactions, making aggregates with higher fractal dimensions.

2.5 Interaction between particles

According to the DLVO theory the total interaction energy $\Phi_{DLVO}(h)$ between two smooth and homogeneous surfaces can be estimated as the sum of the electrostatic repulsion energy arising from the interaction of electrical double layers, the attractive van der Waals forces, and the Born repulsion energy (Loveland et al., 1996):

$$\Phi_{DLVO}(h) = \Phi_{vdW}(h) + \Phi_{dl}(h) + \Phi_{Born}(h) \tag{23}$$

where Φ_{vdW} [J] is the van der Waals energy estimated by the relationship reported by Gregory (1981), Φ_{dl} [J] is the electrostatic interaction energy estimated by the relationship reported by Hogg et al. (1966), Φ_{Born} [J], is the Born interaction energy estimated by the relationship provided by Ruckenstein & Prieve (1976), and h [L] is the separation distance between two approaching particle surfaces.

2.6 Filtration theory

The forward rate coefficient found on the right-hand side of equation (5) can be defined as (Sim & Chrysikopoulos, 1995):

$$r_{n_k - n_k^{*(r)}} = U\Phi F\left(n_k^*\right) \tag{24}$$

where Φ [1/L] is the filter coefficient; $F\left(n_k^*\right)$ [–] is the dynamic blocking function that accounts for porosity variations when particle attachment increases. For submicron particles, such as nanoparticles, it can be assumed that the porous medium is “clean,” and $F\left(n_k^*\right)=1$. The filter coefficient Φ can be calculated as (Rajagopalan & Tien, 1976):

$$\Phi=\frac{3(1-\theta)}{2d_c}\eta \tag{25}$$

where d_c [L] is the average diameter of the collector; and η [–] is the single collector removal efficiency (Yao et al., 1971):

$$\eta=\alpha\eta_o \tag{26}$$

where α [–] is the collision efficiency; and η_o [–] is the single collector contact efficiency, which can be estimated by the correlation developed by Tufenkji and Elimelech (2004). Note that using equations (24)-(26) it is possible to calculate the forward rate coefficient of nanoparticle attachment onto the solid matrix, $r_{n_k-n_k^{*(r)}}$, as a function of the aggregated particle size.

3. Numerical methods

3.1. General solution procedure

The solution of the governing nanoparticle transport equation (1) is quite difficult because multiple physical processes (dispersion, advection, attachment, aggregation) are accounted as a “family” of coupled partial differential equations and in conjunction with equations (2)-(10) a closed system of equations is formed consisting of 3×k unknowns (n_k, $n_k^{*(r)}$, $n_k^{*(i)}$). Every time the total number of classes k_{max} increases by one, three more unknown variables are added along with a new set of equations (1)-(10), making sure the new system is well defined. A direct solution approach for equations (1)-(10) is not possible because the nonlinear PBE equation (2) is coupled to the governing equation (1). Also, conventional numerical approaches would require enormous memory. One efficient alternative method of solution is to decouple the physical processes through operator splitting schemes and solve them one at a time (Barry et al., 2000; Kanney et al., 2003; Steefel & MacQuarrie, 1996; Wood & Baptista, 1993).

The solution approach employed here was to decouple the reactive transport from the aggregation process by using an adaptive double step in conjunction with the symmetrically weighted sequential (SWS) splitting operator method (Botchev et al., 2004). The SWS is a second-order accurate in time scheme. The double adaptive time step allows estimation of the local error by either executing one time-step of size Δt or two sequential steps of size $\Delta t/2$. Therefore, depending on the resulting relative error of these two steps, Δt was adjusted to meet specific criteria. The decoupled processes were solved separately. First, the transport equation (1), without the aggregation source/sink term $(A_n)_k$ and the attachment term $(\rho_b/\theta)(\partial n_k^*/\partial t)$, was solved using the implicit second-order Crank-Nicolson scheme. Next, the resulting concentration values were updated by an iterative process, which involved the solution of equations (4)-(6) for the attachment process (Kinzelbach et al., 1991). Finally, the aggregation process described by equation (2) was solved with subroutine Dodesol (Intel® Ordinary Differential Equations Solver Library), which in conjunction with the SWS scheme, is capable of solving systems of ordinary differential equations with a variable or a priori unknown stiffness.

3.2. Number of clusters

The Smoluchowski equation (2) describes the particle aggregation process, but it does not set explicitly an upper limit on the number of clusters that may occur. As the aggregation process progresses, larger nanoparticles are created. However, the solution of the Smoluchowski equation with a differential equation solver requires a finite number of clusters. There is no limitation how big the max number of clusters, k_{max}, can be, because everytime the number of unknowns (n_k, $n_k^{*(r)}$, $n_k^{*(i)}$) increases so does the number of available equations and the system remains closed. Because there is an exponential relation between the number of clusters and the number of calculations needed, k_{max} should be as small as possible. In this work k_{max} was selected by repeating the same simulation multiple times, while each time the k_{max} value was progressively increased until a subsequent increase in the

k_{max} value did not alter significantly the resulting breakthrough curves. The accepted maximum relative error on the non-negligible concentrations between different simulations for the selected k_{max} was lower than <2%.

4. Model simulations and discussion

4.1 Numerical model verification

The present nanoparticle transport model was compared against: (i) a simple aggregation process under batch conditions (without transport), to validate the accuracy of the numerical methods used for the solution of the aggregation process; and (ii) a simple transport simulation (without aggregation) carried out with the commercial software Comsol™, to ensure that the transport was accurately solved. For the first comparison the aggregation equation (2) with kernel $b_{i,j} = 1$ was compared to the following analytical solution (Smoluchowski, 1916):

$$n_k(k,t) = \left(1 + \frac{t}{2}\right)^{-2} \left(\frac{t}{2+t}\right)^{k-1} \quad (27)$$

The resulting dimensionless concentrations (n_k / n_1^0) are shown in Figure 1a for two different clusters (k=10, 20). Clearly, there is a perfect match between the analytical and numerical solution. For the second comparison, a hypothetical one-dimensional aquifer with length L_x=0.6 m and cross-section A_c=4.91×10^{-4} m^2, consisting of sand grains (collectors) with diameter $d_c = 6 \times 10^{-4}$ m was considered. Subsequently, this hypothetical aquifer will be referred to as "1-D aquifer". A constant number concentration n_1^0=1×10^3 np_1/m^3 entered the 1-D aquifer at x=0 m, for a time period of t_p=15 hr. The model simulations were conducted with $(D_x)_n$=0.09 [m/hr^2], $r_{n_k - n_k^{*(r)}}$=0.25 [1/hr^2], $r_{n_k^{*(r)} - n_k}$=0.01 [1/hr^2], U=0.3 [m/hr^2] and G(t)=0 [np_k/t] and other required parameter values listed in Table 1. All aggregate clusters were assigned the same dispersion coefficient and forward attachment rate, in order to have a direct comparison with the Comsol™ transport model. Note that the Comsol™ model employed the same equations used in the numerical model developed here, but the term $\left(A_n\right)_k(t,x)$ in equation (1), which describes nanoparticle aggregation, was removed. The resulting dimensionless breakthrough concentrations (n_1^T / n_1^0), shown in Figure 1b, are in perfect agreement with the results from the present nanoparticle transport model. Note that n_1^T [np1/L^3] is the total number concentration of suspended nanoparticles (sum of nanoparticles initially present in cluster k=1, which at subsequent times contribute to formation of aggregates in various clusters), and n_1^0 [np1/L^3] is the initially injected number concentration of particles that belong to cluster k=1.

4.2 Attachment rate

Assuming that the attachment of nanoparticles onto collector grains is controlled mainly by the collision efficiency, the forward rate coefficient of reversible nanoparticle attachment onto the solid matrix, $r_{n_k - n_k^{*(r)}}$, as described by the filtration theory (FT) equations (24)-(26), can be calculated for any cluster k and $\left(d_P\right)_k$. For illustration purposes, the coefficient $r_{n_k - n_k^{*(r)}}$ was calculated as a function of $\left(d_P\right)_k$ for a collision efficiency α=0.0048 [-], a collector grain diameter $d_c = 6 \times 10^{-4}$ m, two interstitial velocities (U=0.2, 0.3 m/hr). Furthermore, the collision efficiency, α=0.0048 [-], represents the average of multiple experimental values reported by Syngouna & Chrysikopoulos (2012). All other required parameter values are listed in Table 1. Note that velocity effects are beyond the scope of this work, and only a narrow range of velocities are used in the simulations of this study (U=0.2, 0.3 m/hr). The results are presented in Figure 2 and indicate that $r_{n_k - n_k^{*(r)}}$ decreases to a minimum value at $\left(d_P\right)_1$=850 nm. Beyond this minimum the coefficient $r_{n_k - n_k^{*(r)}}$ increases monotonically with increasing $\left(d_P\right)_k$. Therefore, particles with $\left(d_P\right)_1 < 850$ nm are expected to exhibit reduction in the attachment rate with increasing particle diameter, whereas particles with

$(d_p)_1$ >850 nm are expected to exhibit an increase in the attachment rate with increasing particle diameter. Note that Figure 2 resembles the single-collector efficiency plot reported by Yao et al. (1971), because the forward attachment rate coefficient is linearly correlated with the single-collector efficiency (see equations (24)-(26)).

4.3 Broadpulse source

The present nanoparticle model (equations (1)-(9), (11), (12), (14), (19)) accounting for combined reversible and irreversible attachment, assuming diffusion-limited aggregation (DLA or fast aggregation) with successful collisions calculated by use of the kernel b_{ij}^{DLA} (equation (15)), was applied to the 1-D aquifer, assuming that nanoparticles with diameter $(d_p)_1$ =25 nm enter the aquifer at x=0 m, in a form of a broadpulse over the duration of $t_p = 28$ hr. The forward reversible attachment rate for k=1 was set to $r_{n_1-n_1^{*(r)}}$=0.229 1/hr, and irreversible attachment was neglected ($r_{n_k-n_k^{*(i)}}$=0 1/hr). The collision efficiency was calculated as the average of multiple experimental values reported by Syngouna & Chrysikopoulos (2012), α=0.0048 [-]. All other required model parameter values were those listed in Table 1. In addition, the model developed by Katzourakis and Chrysikopoulos (2015) (subsequently, this biocolloid transport model will be referred to as "KC model") was also applied to the 1-D aquifer under the same conditions with the exception that the attachment rate was assumed independent of aggregate size and equal to $r_{n-n^{*(r)}}$= 0.229 [1/hr]. Note that the KC model describes the transport of colloids in three-dimensional, water saturated, homogeneous porous media, accounting for particle attachment onto the solid matrix by the two-site kinetic model, without considering particle aggregation.

In Figure 3a-f are shown the dimensionless concentrations as simulated by both the present nanoparticle transport model and the KC model, at three different locations within the 1-D aquifer (x=0.2, 0.35, and 0.6 m) as a function of time (see Figures 3a-c), and at three different times (t=3, 28, and 32 hr) as a function of distance within the aquifer (see Figure 3d-f). The concentrations simulated by the present nanoparticle transport model reach peak concentrations faster, and exhibit less pronounced tailing than the KC model (see Figure 3a-c). Also, the nanoparticle distribution (snapshots) within the 1-D aquifer as simulated by the present nanoparticle transport model is higher at early times (t=3 hr) and lower at late times (t=32 hr) compared to the KC model (see Figure 3d, and f). As the aggregate diameters increase the various attachment rates $r_{n_k - n_k^{*(r)}}$ decrease (there is a different attachment rate for each cluster). When the nanoparticle attachment rate is reduced, fewer nanoparticles are retained by the solid matrix of the aquifer. It should be noted that for the simulations in Figures 3a-f the aggregate diameters did not exceed $(d_p)_1 =$386 nm.

The simulations presented in Figure 3a-f were repeated for the case where only irreversible attachment was accounted for. In the present nanoparticle transport model, the reversible attachment and detachment rates were set to zero ($r_{n_k^{*(r)} - n_k} = r_{n_k - n_k^{*(r)}} = 0$ 1/hr), and the irreversible attachment to $r_{n_1 - n_1^{*(i)}}$ =0.229 1/hr. In the KC model, the reversible attachment and detachment rates were set to zero, and the irreversible attachment was set to $r_{n - n^{*(i)}}$ =0.229 1/hr. The simulations for the case where only irreversible attachment was accounted for, are presented in Figure 3g-l. Note that the results from the simulations obtained by the two models are quite different. The present nanoparticle transport model consistently yielded dimensionless total number concentrations significantly higher than those of the KC model. This discrepancy is attributed to nanoparticle aggregation, which is accounted for in the present nanoparticle transport model. As nanoparticles aggregate, new clusters with larger aggregates are created. A different $r_{n_k - n_k^{*(i)}}$ rate is assigned to each cluster, with a value which is decreasing with increasing cluster number. The effect of aggregation is more pronounced when irreversible attachment is accounted for, than when reversible attachment is considered (compare Figures 3a-f and 3g-l). This observation suggests that the nanoparticle aggregation effect on transport could be masked when reversible attachment occurs. This is similar to the findings reported in the literature that reversible attachment may conceal the effects of the geochemical heterogeneity of an aquifer (Katzourakis & Chrysikopoulos, 2018).

The dimensionless average size of the suspended aggregates, $\bar{d}_P/(d_P)_1$ [-], for the exact conditions examined in Figures 3a-f, are presented in Figure 4. The trend of the $\bar{d}_P/(d_P)_1$ for the case where there is reversible attachment, shown in Figures 4a-c are very similar to those shown for n_1^T/n_1^0 in Figures 3a-c. Clearly, the aggregate size is directly proportional to the nanoparticle concentration. The ratio $\bar{d}_P/(d_P)_1$ increases considerably, up to a seven-fold. The increase in $\bar{d}_P/(d_P)_1$ with distance along the 1-D aquifer observed in Figures 4d-f is expected, because as the nanoparticles move downstream they aggregate and consequently increase in size. A temporary increase in $\bar{d}_P/(d_P)_1$ appears immediately after the broad pusle injection of nanoparticles is completed ($t>t_p$=28 hr, see Figures 4a-c), because particles previously attached onto the solid matrix with size greater or equal to the injected nanoparticles $\left((d_P)_k \geq (d_P)_1\right)$ are starting to detach. This increase in $\bar{d}_P/(d_P)_1$ fades away with time as the nanoparticle concentration reduces rapidly. For the case where irreversible attachment is considered and at times $t>t_p$ the ratio $\bar{d}_P/(d_P)_1$ becomes negligible after a temporary sharp increase. This is a consequence of the faster irreversible attachement of smaller sized nanoparticles, which in turn leads to an increase in the average size of the suspended aggregates. Note that for relatively small nanoparticles, the attachment rate is inversely proportional to their aggregate size (see Figure 2). Also, the suspended nanoparticle number concentrations eventually become negligible due to irreversible attachment. In contrast, for the case where reversible attachment is considered, the reduction of smaller aggregates is less pronounced because there are continuously detached. This is the reason that at late times (t=32 hr, Figure 4f) the ratio $\bar{d}_P/(d_P)_1$ is substantially higher for the case where irreversible attachment is considered.

4.4 Instantaneous source

The present nanoparticle model with instantaneous source (equations (1)-(8),(10),(11),(13),(14),(19)) and the KC model with instantaneous source, assuming diffusion-limited aggregation (DLA or fast aggregation) with successful collisions calculated by use of the kernel b_{ij}^{DLA} (equation (15)), were used to simulate nanoparticle transport in the 1-D aquifer. Two different nanoparticle diameters were considered: $(d_p)_1$ =25 nm, and $(d_p)_1$ =850 nm. Each size of nanoparticles was examined separately. The nanoparticles were introduced instantaneously in the aquifer at x_0=0.10 m. The number of nanoparticles injected was $(N_{inj})_1 = 3\times10^{10}$ [np_1] for both nanoparticle sizes. For the present nanoparticle transport model the forward reversible attachment rate for k=1 was $r_{n_1-n_1^{*(r)}}$ =0.257 1/hr for $(d_p)_1 = 25$ nm, and $r_{n_1-n_1^{*(r)}}$=0.0227 1/hr for $(d_p)_1$ =850 nm (see Figure 2). For the KC model the forward reversible attachment rate was set to $r_{n-n^{*(r)}}$=0.257 1/hr for $(d_p)_1$ =25 nm and $r_{n-n^{*(i)}}$ =0.0227 1/hr for $(d_p)_1 = 850$ nm. All other required model parameters were those listed in Table 1. The model simulations are presented in Figure 5. As expected, the total number concentrations (n_1^T) decrease with increasing time and distance from the source location. For the smaller nanoparticles ($(d_p)_1 = 25$ nm) the simulated n_1^T curves were higher for the present transport model than the KC model (see Figures 5a,b). However, for the larger nanoparticles ($(d_p)_1$ =850 nm) the simulated n_1^T curves were lower for the present transport model than the KC model (see Figures 5c,d). For both nanoparticle sizes considered here, the difference between the n_1^T curves simulated with the present transport model and the KC model, increases with increasing time and distance. These observations are attributed to the aggregate diameter increase, which is only accounted by the present model. Note that for the smaller nanoparticles the attachment rate

$r_{n_k - n_k^{*}(r)}$ decreases as the aggregate diameter increases, while for the larger nanoparticles the opposite is true (see Figure 2). Therefore, when the mean of the various $r_{n_k - n_k^{*}(r)}$ values decreases, n_1^T increases and when the mean of the various $r_{n_k - n_k^{*}(r)}$ values increases, n_1^T decreases.

The dimensionless average size distributions of suspended aggregates, $\bar{d}_P / \left(d_P\right)_1$ [-], for the exact conditions examined in Figures 5, are presented in Figure 6. The $\bar{d}_P / \left(d_P\right)_1$ trend for the smaller nanoparticles ($(d_P)_1 = 25$ nm) follows the trend of n_1^T shown in Figures 5a,b. Positive n_1^T slopes lead to increasing $\bar{d}_P / \left(d_P\right)_1$ ratios and negative n_1^T slopes to decreasing $\bar{d}_P / \left(d_P\right)_1$ ratios. However, upstream from the source location (x_0=0.1 m), the dashed curve in Figure 6e exhibits a dip (minimum), which is not observed in the corresponding n_1^T curve in Figure 5b. Near the source, the $(d_P)_1 = 25$ nm nanoparticles, which have diffused upstream, attach onto the solid matrix of the 1-D aquifer with greater attachment rate than the constantly forming larger aggregates (see Figure 2). When the suspended nanoparticles migrate away from the source, the attached smaller nanoparticles detach, and in turn contribute to the reduction of the $\bar{d}_P / \left(d_P\right)_1$ ratio, as shown by the dip in the dashed curve of Figure 6e. At a subsequent point in time (t=1.1 hr), this dip is smoothed because the $\bar{d}_P / \left(d_P\right)_1$ ratio upstream from the source location is reduced due to the nanoparticle migration (see dashed curve in Figure 6f). It should be noted that at late times, the $\bar{d}_P / \left(d_P\right)_1$ trend of the nanoparticles with diameter $(d_P)_1$ =850 nm (see Figure 6a-c) deviates significantly from the trend of n_1^T shown in Figures 5c,d. This is attributed to the increasing attachment as nanoparticles with $(d_P)_1$ =850 nm form larger aggregates (see Figure 2). At late times, when n_1^T decreases due to nanoparticle transport and attachment onto the solid matrix of the porous medium, some large aggregates detach and contribute to the observed increase in $\bar{d}_P / \left(d_P\right)_1$. Note that the snapshots for $(d_p)_1$ =850 nm (solid curves) in Figures 6e,f exhibit two distinct peaks. The second peak further downstream is expected, because it follows the n_1^T trend (Figure 5d). However, the first peak, near the source location (x_0=0.1 m), is attributed to formation of larger aggregates with attachment rates that increase as their size increases (see Figure 2). These aggregates detach from the solid matrix after the main concentration peak migrates downstream.

4.5 Nanoparticle size-dependent dispersivity

The hydrodynamic dispersion is an important transport parameter and for aggregating nanoparticles should not be considered as an invariant parameter, but different clusters should be assigned different values:

$$(D_x)_k = \alpha_L U \tag{28}$$

where α_L [L] is the longitudinal dispersivity. As the size of nanoparticles increase their dispersivity is also increasing, because as the size of particles increases: (1) the particle effective porosity is reduced, and (2) particles are excluded from lower-velocity regions of the parabolic velocity profile within the pore throats (Chrysikopoulos & Katzourakis, 2015).

To illustrate the effect of size-dependent dispersivity the simulations presented in Figure 5c were repeated under the exact same conditions with only one difference, the present nanoparticle transport model was modified to account for size-dependent dispersivity. It was assumed that aggregate dispersivity is increasing with particle diameter based on the following empirical relationship (Chrysikopoulos & Katzourakis, 2015):

$$\alpha_L[\mathrm{cm}] = 0.29 + 5.06\times10^{-5}\, d_p[\mathrm{nm}] \tag{29}$$

In present nanoparticle transport model the dispersion was estimated by equations (28) and (29) (i.e. k=1, $(d_p)_1 = 850$ nm, $(D_x)_1 = 1\times10^{-3}$ m/hr^2), whereas in the KC model the dispersion coefficient was set to $D_x = 1\times10^{-3}$ m/hr^2. The simulated number concentration of suspended nanoparticle, n_1^T, breakthrough curves are presented in Figure 7. It is shown that simulations conducted with the present nanoparticle transport model, which accounts for size-dependent dispersivity exhibit early breakthrough, more spreading, extended tailing, and lower concentrations compared to the KC model. This result is expected, because formation of aggregates with progressively increasing diameter size result in increasing dispersion coefficients.

4.6 Comparison between DLA and RLA

The simulations presented in Figure 5c, under the assumption of diffusion-limited aggregation (DLA or fast aggregation), were repeated for the exact same conditions, but assuming reaction-limited aggregation (RLA or slow aggregation) with successful collisions determined by use of the kernel b_{ij}^{RLA} (equation (16)). For the RLA simulations, the surface potential of the particles of cluster k=1 containing nanoparticles with diameter $(d_p)_1$ =850 nm was set to Ψ_{p1}=8.7 [mV]. Also, the dispersivity was assumed to be invariant with aggregate size.

The simulated breakthrough curves of the total number concentration of suspended nanoparticles, n_1^T, obtained by the present model assuming RLA are presented in Figure 8, together with the corresponding breakthrough curves obtained by the present model assuming DLA, and the KC model. Clearly, the breakthrough curves simulated under the assumption of RLA are higher than those simulated under the assumption of DLA, but lower that those obtained by the KC model. This is an expected result because fewer aggregates are formed with RLA than DLA, and the KC model neglects aggregation. Note that for nanoparticles with diameter $(d_p)_1 = 850$ nm aggregate formation leads to higher attachment rates (see Figure 2).

4.7 Impact of fractal dimension D_F on nanoparticle transport

To further investigate the effect of nanoparticle aggregation on nanoparticle transport, the simulations presented in Figure 5c for diffusion-limited aggregation (DLA or fast aggregation), were repeated for different fractal dimension values (D_F). The number of nanoparticles injected was $(N_{inj})_1 = 3\times10^{10}$ [np1] with diameter $(d_p)_1$ =850 nm. The results are presented in Figure 9.

It is evident from Figure 9 that as the value of D_F decreases the average concentration decreases as well. This is expected because larger D_F values correspond to smaller cluster diameters (see equation (19)), which in turn leads to smaller average attachment rates (see Figure 2). Therefore, smaller D_F values yield higher attachment rates and smaller concentrations. Note that the KC model concentrations can differ from the current model concentrations up to an order of magnitude. Consequently, the effects of aggregation cannot be overlooked.

4.8 Comparison to other studies

The results presented in this work are in agreement with other studies published in the literature. Raychoudhury et al. (2012) performed various nanoparticle transport experiments in columns packed with sand, and pointed out that the particle single collector contact efficiency changes with particle diameter. It was reported that initially the increasing particle size led to decreasing collector efficiency; subsequently, as the particle size increased further, the collector efficiency increased, following a trend similar to the one shown in Figure 2. Using this relationship between particle size and collector efficiency, model simulations with the Smoluchowski equation were performed, which indicated, as in the present study (Figure 3c,i), that breakthrough concentrations of small aggregating particles were higher than non-aggregating particles. Also, Taghavy et al. (2015) obtained the same result by developing a Lagrangian model that accounted for aggregation and incorporated the population balance equation (2). Contrarily, Babakhani (2019) reported that for a specific size range of nanoparticles when aggregation was accounted for, the breakthrough concentration decreased (as also shown in Figure 5c). The differences in the results presented by the various authors are caused by the attachment behaviour, because an increase in nanoparticle aggregate size may lead to either increased or decreased attachment (see Figure 2). Finally, despite some differences in the modelling of the attachment process (kinetic, equilibrium, DLVO interactions), all of these studies concluded that aggregation can change the average attachment rate and in turn can affect the mobility of nanoparticles, as reported in this work.

5. Summary and conclusions

The novel nanoparticle transport model was developed in this work accounts for advection, dispersion, reversible and irreversible attachment, and aggregation. Both DLA and RLA conditions were considered. For the numerical solution, the transport and attachment processes were decoupled from the aggregation process using an adaptive splitting operator method and then were solved separately. The results from numerous simulations suggested that nanoparticle aggregation affects significantly nanoparticle transport in porous media. It was shown that due to aggregation the size of nanoparticles increases, which in turn can lead to an increased or decreased average attachment rate, depending on the initial particle diameter. An increase in average attachment causes late breakthrough, while a decrease yields early breakthrough. Particle size-dependant dispersivity enhances spreading and leads to early breakthrough of nanoparticles. The effect of nanoparticle aggregation was more pronounced for irreversible than reversible attachment. Also, it was shown that the effects of aggregation were more significant under DLA than RLA conditions. The discrepancies between the transport with and without aggregation varied in time and space and were more evident as the evolution of aggregation progressed further. Therefore, for the simulation of nanoparticle transport in porous media, neglecting to account for aggregation, particle-size dependent dispersivity or particle surface charges, can lead to erroneous and unrealistic results.

Acknowledgments: This research has received funding from the Partnership for Research and Innovation in the Mediterranean Area (PRIMA), under grant agreement number: 1923-InTheMED. FAIR data policy statement: All figures and tables can be directly reproduced from the equations presented in this manuscript.

6. References

Arosio, P., Rima, S., Lattuada, M., & Morbidelli, M. (2012). Population balance modeling of antibodies aggregation kinetics. *The Journal of Physical Chemistry B*, *116*(24), 7066–7075. https://doi.org/10.1021/jp301091n

Axford, S. D. (1997). Aggregation of colloidal silica: Reaction-limited kernel, stability ratio and distribution moments. *J. Chem. Soc., Faraday Trans.*, *93*(2), 303–311. https://doi.org/10.1039/A606195H

Babakhani, P. (2019). The impact of nanoparticle aggregation on their size exclusion during transport in porous media: One-and three-dimensional modelling investigations. Scientific Reports, 9(1), 1–12. https://doi.org/10.1038/s41598-019-50493-6

Babakhani, P., Bridge, J., Phenrat, T., Fagerlund, F., Doong, R., & Whittle, K. R. (2019). Comparison of a new mass-concentration, chain-reaction model with the population-balance model for early-and late-stage aggregation of shattered graphene oxide nanoparticles. Colloids and Surfaces A: Physicochemical and Engineering Aspects, 582, 123862. https://doi.org/10.1016/j.colsurfa.2019.123862

Babakhani, P., Doong, R., & Bridge, J. (2018). Significance of early and late stages of coupled aggregation and sedimentation in the fate of nanoparticles: Measurement and modeling. Environmental Science & Technology, 52(15), 8419–8428. https://doi.org/10.1021/acs.est.7b05236

Barry, D., Bajracharya, K., Crapper, M., Prommer, H., & Cunningham, C. J. (2000). Comparison of split-operator methods for solving coupled chemical non-equilibrium reaction/groundwater transport models. *Mathematics and Computers in Simulation*, *53*(1–2), 113–127. https://doi.org/10.1016/S0378-4754(00)00182-8

Bedrikovetsky, P., Siqueira, F. D., Furtado, C. A., & Souza, A. L. S. (2011). Modified particle detachment model for colloidal transport in porous media. Transport in Porous Media, 86(2), 353–383. https://doi.org/10.1007/s11242-010-9626-4

Bedrikovetsky, P., Zeinijahromi, A., Siqueira, F. D., Furtado, C. A., & de Souza, A. L. S. (2012). Particle detachment under velocity alternation during suspension transport in porous media. Transport in Porous Media, 91(1), 173–197. https://doi.org/10.1007/s11242-011-9839-1

Benn, T., & Westerhoff, P. (2008). Nanoparticle silver released into water from commercially available sock fabrics. *Environmental Science and Technology*, *42*(11), 4133–4139. https://doi.org/10.1021/es7032718

Botchev, M., Faragó, I., & Havasi, Á. (2004). Testing weighted splitting schemes on a one-column transport-chemistry model. International Journal of Environment and Pollution, 22(1–2), 3–16. https://doi.org/10.1504/ijep.2004.005473

Brar, S., Verma, M., Tyagi, R. D., & Surampalli, R. Y. (2010). Engineered nanoparticles in wastewater and wastewater sludge - Evidence and impacts. *Waste Management*, *30*(3), 504-520. https://doi.org/10.1016/j.wasman.2009.10.012

Chatterjee, J., & Gupta, S. K. (2009). An agglomeration-based model for colloid filtration. Environmental Science and Technology, 43(10), 3694–13699. https://doi.org/10.1021/es8029973

Chen, G., Liu, X., & Su, C. (2011). Transport and retention of TiO2 rutile nanoparticles in saturated porous media under low-ionic-strength conditions: Measurements and mechanisms. *Langmuir*, *27*(9), 5393–5402. https://doi.org/10.1021/la200251v

Chowdhury, I., Hong, Y., Honda, R. J., & Walker, S. L. (2011). Mechanisms of TiO2 nanoparticle transport in porous media: Role of solution chemistry, nanoparticle concentration, and flowrate. *Journal of Colloid and Interface Science*, *360*(2), 548–555. https://doi.org/10.1016/j.jcis.2011.04.111

Chrysikopoulos, C. V., & Katzourakis, V. E. (2015). Colloid particle size-dependent dispersivity. *Water Resources Research*, *51*(6), 4668–4683. https://doi.org/10.1002/2014WR016094

Chrysikopoulos, C. V., & Syngouna, V. I. (2012). Attachment of bacteriophages MS2 and ΦX174 onto kaolinite and montmorillonite: Extended-DLVO interactions. *Colloids and Surfaces B: Biointerfaces*, *92*, 74–83. https://doi.org/10.1016/j.colsurfb.2011.11.028

Compère, F., Porel, G., & Delay, F. (2001). Transport and retention of clay particles in saturated porous media. Influence of ionic strength and pore velocity. *Journal of Contaminant Hydrology*, *49*(1–2), 1–21. https://doi.org/10.1016/S0169-7722(00)00184-4

Elimelech, M., & O'Melia, C. R. (1990). Kinetics of Deposition of Colloidal Particles in Porous Media. *Environmental Science and Technology*, *24*(10), 1528–1536. https://doi.org/10.1021/es00080a012

Family, F., Meakin, P., & Vicsek, T. (1985). Cluster size distribution in chemically controlled cluster-cluster aggregation. The Journal of Chemical Physics, 83(8), 4144–4150. https://doi.org/10.1063/1.449079

Fang, J., Shan, X. Q., Wen, B., Lin, J. Ming, & Owens, G. (2009). Stability of titania nanoparticles in soil suspensions and transport in saturated homogeneous soil columns. *Environmental Pollution*, *157*(4), 1101–1109. https://doi.org/10.1016/j.envpol.2008.11.006

Feder, J. (1988). Fractals New York. Plenum Press.

Feke, D. L., Prabhu, N. D., Mann, J. A., & Mann, J. A. (1984). A formulation of the short-range repulsion between spherical colloidal particles. Journal of Physical Chemistry, 88(23), 5735–5739. https://doi.org/10.1021/j150667a055

Fuchs, N. (1934). About the stability and loading of aerosols. *Journal of Physics*, *89*(11–12), 736–743.

Gaudreault, R., Di Cesare, N., Van De Ven, T. G. M., & Weitz, D. A. (2015). Structure and Strength of Flocs of Precipitated Calcium Carbonate Induced by Various Polymers Used in Papermaking. *Industrial and Engineering Chemistry Research*, *54*(24), 6234–6246. https://doi.org/10.1021/acs.iecr.5b00818

Godinez, I. G., & Darnault, C. J. G. (2011). Aggregation and transport of nano-TiO2 in saturated porous media: Effects of pH, surfactants and flow velocity. *Water Research*, *45*(2), 839–851. https://doi.org/10.1016/j.watres.2010.09.013

Goldberg, E., Scheringer, M., Bucheli, T. D., & Hungerbühler, K. (2014). Critical Assessment of Models for Transport of Engineered Nanoparticles in Saturated Porous Media. *Environmental Science & Technology*, *48*(21), 12732–12741. https://doi.org/10.1021/es502044k

Gottschalk, F., Sonderer, T., Scholz, R. W., & Nowack, B. (2009). Modeled environmental concentrations of engineered nanomaterials (TiO2, ZnO, Ag, CNT, fullerenes) for different regions. *Environmental Science and Technology*, *43*(24), 9216–9222. https://doi.org/10.1021/es9015553

Gregory, J. (1981). Approximate expressions for retarded van der Waals interaction. *Journal of Colloid and Interface Science*, *83*(1), 138–145. https://doi.org/10.1016/0021-9797(81)90018-7.

Heidmann, I. (2013). Metal oxide nanoparticle transport in porous media – an analysis about (un)certainties in environmental research. *Journal of Physics: Conference Series*, *429*, 012042. https://doi.org/10.1088/1742-6596/429/1/012042

Hogg, R., Healy, T. W., & Fuerstenau, D. W. (1966). Mutual coagulation of colloidal dispersions. *Transactions of the Faraday Society*, *62*, 1638–1651. https://doi.org/10.1039/tf9666201638

IARC (2010) Monographs on the evaluation of carcinogenic risks to humans, v. 93, World Health Organization, 2010

Kanney, J. F., Miller, C. T., & Kelley, C. T. (2003). Convergence of iterative split-operator approaches for approximating nonlinear reactive problems. *Advances in Water Resources*, *26*(3), 247–261. https://doi.org/10.1016/S0309-1708(02)00162-8

Katzourakis, V. E., & Chrysikopoulos, C. V. (2014). Mathematical modeling of colloid and virus cotransport in porous media: Application to experimental data. *Advances in Water Resources*, *68*, 62–73. https://doi.org/10.1016/j.advwatres.2014.03.001

Katzourakis, V. E., & Chrysikopoulos, C. V. (2015). Modeling dense-colloid and virus cotransport in three-dimensional porous media. *Journal of Contaminant Hydrology*, *181*, 102–113. https://doi.org/10.1016/j.jconhyd.2015.05.010

Katzourakis, V. E., & Chrysikopoulos, C. V. (2018). Impact of Spatially Variable Collision Efficiency on the Transport of Biocolloids in Geochemically Heterogeneous Porous Media. Water Resources Research, 54(6), 3841–3862. https://doi.org/10.1029/2017WR021996

Kinzelbach, W., Schäfer, W., & Herzer, J. (1991). Numerical modeling of natural and enhanced denitrification processes in aquifers. *Water Resources Research*, *27*(6), 1123–1135. https://doi.org/10.1029/91WR00474

Lattuada, M., Sandkühler, P., Wu, H., Sefcik, J., & Morbidelli, M. (2003). Aggregation kinetics of polymer colloids in reaction limited regime: experiments and simulations. *Advances in Colloid and Interface Science*, *103*(1), 33–56. https://doi.org/10.1016/S0001-8686(02)00082-9

Lee, D. G., Bonner, J. S., Garton, L. S., Ernest, A. N. S., & Autenrieth, R. L. (2000). Modeling coagulation kinetics incorporating fractal theories: A fractal rectilinear approach. *Water Research*, *34*(7), 1987–2000. https://doi.org/10.1016/S0043-1354(99)00354-1

Lin, M. Y., Klein, R., Lindsay, H. M., Weitz, D. A., Ball, R. C., & Meakin, P. (1990). The structure of fractal colloidal aggregates of finite extent. *Journal of Colloid And Interface Science*, *137*(1), 263–280. https://doi.org/10.1016/0021-9797(90)90061-R

Lin, M. Y., Lindsay, H. M., Weitz, D. A., Ball, R. C., Klein, R., & Meakin, P. (1989). Universality in colloid aggregation. *Nature*, *339*(6223), 360–362. https://doi.org/10.1038/339360a0

Litton, G. M., & Olson, T. M. (1996). Particle size effects on colloid deposition kinetics: Evidence of secondary minimum deposition. *Colloids and Surfaces A: Physicochemical and Engineering Aspects*, *107*, 273–283. https://doi.org/10.1016/0927-7757(95)03343-2

Liu, H. H., Surawanvijit, S., Rallo, R., Orkoulas, G., & Cohen, Y. (2011). Analysis of nanoparticle agglomeration in aqueous suspensions via constant-number Monte Carlo simulation. *Environmental Science and Technology*, *45*(21), 9284–9292. https://doi.org/10.1021/es202134p

Loveland, J. P., Ryan, J. N., Amy, G. L., & Harvey, R. W. (1996). The reversibility of virus attachment to mineral surfaces. In *Colloids and Surfaces A: Physicochemical and Engineering Aspects*, 107, 205–221. https://doi.org/10.1016/0927-7757(95)03373-4

Marray, J. P., & Parks, G. A. (1978). Particulates in Water: Characterization, Fate, Effects and Removal, edited by MC Kavanaugh and JO Leckie. Adv. Chem. Ser., Amican Chemical Society, Washington, DC, USA, 189.

Mueller, N. C., & Nowack, B. (2008). Exposure modelling of engineered nanoparticles in the environment. *Environmental Science & Technology*, *42*(12), 44447–53. https://doi.org/10.1021/es7029637

Nicoud, L., Arosio, P., Sozo, M., Yates, A., Norrant, E., & Morbidelli, M. (2014). Kinetic analysis of the multistep aggregation mechanism of monoclonal antibodies. Journal of Physical Chemistry B, 118(36), 10595–10606. https://doi.org/10.1021/jp505295j

Nowack, B., & Bucheli, T. D. (2007). Occurrence, behavior and effects of nanoparticles in the environment. Environmental pollution, 150(1), 5-22. https://doi.org/10.1016/j.envpol.2007.06.006

Petosa, A. R., Jaisi, D. P., Quevedo, I. R., Elimelech, M., & Tufenkji, N. (2010). Aggregation and deposition of engineered nanomaterials in aquatic environments: role of

physicochemical interactions. Environmental Science & Technology, 44(17), 6532–6549. https://doi.org/10.1021/es100598h
Quik, J.T., de Klein, J.J. and Koelmans, A.A., (2015). Spatially explicit fate modelling of nanomaterials in natural waters. Water research, 80, .200-208. http://dx.doi.org/10.1016/j.watres.2015.05.025
Rajagopalan, R., & Tien, C. (1976). Trajectory analysis of deep-bed filtration with the sphere-in-cell porous media model. *AIChE Journal*, *22*(3), 523–533. https://doi.org/10.1002/aic.690220316
Raychoudhury, T., Tufenkji, N., & Ghoshal, S. (2012). Aggregation and deposition kinetics of carboxymethyl cellulose-modified zero-valent iron nanoparticles in porous media. Water research, 46(6), 1735-1744.
Reerink, H., & Overbeek, J. T. G. (1954). The rate of coagulation as a measure of the stability of silver iodide sols. *Discussions of the Faraday Society*, *18*, 74. https://doi.org/10.1039/df9541800074
Ruckenstein, E., & Prieve, D. C. (1976). Adsorption and desorption of particles and their chromatographic separation. *AIChE Journal*, *22*(2), 276–283. https://doi.org/10.1002/aic.690220209
Russell, T., & Bedrikovetsky, P. (2018). Colloidal-suspension flows with delayed fines detachment: Analytical model & laboratory study. Chemical Engineering Science, 190, 98–109. https://doi.org/10.1016/j.ces.2018.05.062
Ryan, J. N., & Gschwend, P. M. (1994). Effects of ionic strength and flow rate on colloid release: Relating kinetics to intersurface potential energy. *Journal of Colloid and Interface Science*, *164*, 21–34. https://doi.org/10.1006/jcis.1994.1139
Sabelfeld, K., & Kolodko, A. (2002). Stochastic Lagrangian models and algorithms for spatially inhomogeneous Smoluchowski equation. *Mathematics and Computers in Simulation*, *61*(2), 115–137. https://doi.org/10.1016/S0378-4754(02)00141-6
Sandkühler, P., Sefcik, J., & Morbidelli, M. (2004). Kinetics of aggregation and gel formation in concentrated polystyrene colloids. *The Journal of Physical Chemistry B*, *108*(52), 20105–20121. https://doi.org/10.1021/jp046468w
Shamir, U. Y., & Harleman, D. R. F. (1967). Numerical solutions for dispersion in porous mediums. *Water Resources Research*, *3*(2), 557–581. https://doi.org/10.1029/WR003i002p00557
Sim, Y., & Chrysikopoulos, C. (1998). Three-dimensional analytical models for virus transport in saturated porous media. *Transport in Porous Media*, *30*(1), 87–112. https://doi.org/10.1023/A:1006596412177
Sim, Y., & Chrysikopoulos, C. V. (1995). Analytical Models for One-Dimensional Virus Transport in Saturated Porous Media. *Water Resources Research*, *31*(5), 1429–1437. https://doi.org/10.1029/95WR00199
Sim, Y., & Chrysikopoulos, C. V. (1999). Analytical solutions for solute transport in saturated porous media with semi-infinite or finite thickness. *Advances in Water Resources*, *22*(5),

507–519. https://doi.org/10.1016/S0309-1708(98)00027-X

Smoluchowski, M. V. (1916). Über Brownsche Molekularbewegung unter Einwirkung äußerer Kräfte und deren Zusammenhang mit der verallgemeinerten Diffusionsgleichung. *Annalen Der Physik*, *353*(24), 1103–1112. https://doi.org/10.1002/andp.19163532408

Smoluchowski, M. V. (1917). Versuch einer mathematischen theorie der koagulation kinetic kolloider losungen. *Zeit. Phys. Chem*, *92*, 129–168.

Smoluchowski, Marian. (1916). Drei Vortrage uber Diffusion. Brownsche Bewegung und Koagulation von Kolloidteilchen. *Z. Phys.*

Solovitch, N., Labille, J., Rose, J., Chaurand, P., Borschneck, D., Wiesner, M. R., & Bottero, J. Y. (2010). Concurrent aggregation and deposition of TiO2 nanoparticles in a sandy porous media. *Environmental Science and Technology*, *44*(13), 4897–4902. https://doi.org/10.1021/es1000819

Steefel, C. I., & MacQuarrie, K. T. B. (1996). Approaches to modeling of reactive transport in porous media. *Reviews in Mineralogy*, *34*(1), 83-129.

Syngouna, V. I., & Chrysikopoulos, C. V. (2012). Transport of biocolloids in water saturated columns packed with sand: Effect of grain size and pore water velocity. *Journal of Contaminant Hydrology*, *129–130*, 11–24. https://doi.org/10.1016/j.jconhyd.2012.01.010

Syngouna, V. I., & Chrysikopoulos, C. V. (2013). Cotransport of clay colloids and viruses in water saturated porous media. *Colloids and Surfaces A: Physicochemical and Engineering Aspects*, *416*(1), 56–65. https://doi.org/10.1016/j.colsurfa.2012.10.018

Taghavy, A., Pennell, K. D., & Abriola, L. M. (2015). Modeling coupled nanoparticle aggregation and transport in porous media: A Lagrangian approach. Journal of contaminant hydrology, 172, 48-60.

Tufenkji, N., & Elimelech, M. (2004). Correlation Equation for Predicting Single-Collector Efficiency in Physicochemical Filtration in Saturated Porous Media. *Environmental Science and Technology*, *38*(2), 529–536. https://doi.org/10.1021/es034049r

Vasiliadou, I. A., & Chrysikopoulos, C. V. (2011). Cotransport of Pseudomonas putida and kaolinite particles through water-saturated columns packed with glass beads. Water Resources Research, 47(2), W02543. https://doi.org/10.1029/2010WR009560

Wang, M., Gao, B., Tang, D., & Yu, C. (2018). Concurrent aggregation and transport of graphene oxide in saturated porous media: roles of temperature, cation type, and electrolyte concentration. Environmental Pollution, 235, 350–357. https://doi.org/10.1016/j.envpol.2017.12.063

Weast, R. C. (1984). *Handbook of Chemistry and Physics 64th Edition 1983-1984*. Boca Raton, FL, USA: CRC Press.

Weitz, D. A., & Lin, M. Y. (1986). Dynamic Scaling of Cluster-Mass Distributions in Kinetic Colloid Aggregation. *Physical Review Letters*, *57*(16), 2037–2040. https://doi.org/10.1103/PhysRevLett.57.2037

Weitz, D. A., Lin, M. Y., & Lindsay, H. M. (1991). Universality laws in coagulation. *Chemometrics and Intelligent Laboratory Systems*, *10*(1–2), 133–140.

https://doi.org/10.1016/0169-7439(91)80043-P

Wiesner, M. R., Lowry, G. V., Alvarez, P., Dionysiou, D., & Biswas, P. (2006). Assessing the risks of manufactured nanomaterials. *Environmental Science and Technology*, 40(14), 4336-4345. https://doi.org/10.1021/es062726m

Wijnen, P. W. J. G., Beelen, T. P. M., Rummens, C. P. J., & van Santen, R. A. (1991). Diffusion- and reaction-limited aggregation of aqueous silicate solutions. *Journal of Non-Crystalline Solids*, *136*(1–2), 119–125. https://doi.org/10.1016/0022-3093(91)90127-R

Wood, T. M., & Baptista, A. M. (1993). A model for diagnostic analysis of estuarine geochemistry. *Water Resources Research*, *29*(1), 51–71. https://doi.org/10.1029/92WR02126

Yao, K., Habibian, M. T., & O'Melia, C. R. (1971). Water and Waste Water Filtration: Concepts and Applications. *Environmental Science & Technology*, *5*(11), 1105–1112. https://doi.org/10.1021/es60058a005

Table 1. Model parameters

Broadpulse Simulations			Instantaneous Simulations		
Parameter	**Value (units)**	**Reference**	**Parameter**	**Value (units)**	**Reference**
$(D_x)_k$ [a]	9×10^{-3} (m^2/hr)	–	U	0.3 (m/hr)	(Chrysikopoulos & Katzourakis, 2015)
U	0.2 (m/hr)	(Syngouna & Chrysikopoulos, 2013)	$(N_{inj})_1$	3×10^{10} (np_1)	–
t_p	28 (hr)	–	$r_{n_k^{*(r)}-n_k}$	0.03 (1/hr)	(Vasiliadou & Chrysikopoulos, 2011)
$(d_p)_1$	25×10^{-9} (m)	–	$r_{n_k-n_k^{*(i)}}$	0 (1/hr)	–
n_1^o [b]	1×10^{15} (np_1/m^3)	–	x_0	0.1 (m)	–
With reversible attachment			*Instantaneous simulations (d_1=25 nm)*		
$r_{n_1-n_1^{*(r)}}$ [c]	0.229 (1/hr)	*Equation* (24)	$(D_x)_k$	8×74^{-4} (m^2/hr)	Equation (28)
$r_{n_k-n_k^{*(i)}}$ [d]	0 (1/hr)	–	$(d_p)_1$	25×10^{-9} (m)	–
$r_{n_k^{*(r)}-n_k}$ [e]	0.3 (1/hr)	(Vasiliadou & Chrysikopoulos, 2011)	$r_{n-n^{*(r)}}$	0.257 (1/hr)	*Equation* (24)
$r_{n-n^{*(r)}}$ [f]	0.229 (1/hr)	*Equation* (24)	$r_{n_1-n_1^{*(r)}}$	0.257 (1/hr)	*Equation* (24)
With irreversible attachment			*Instantaneous simulations (d_1=850 nm)*		
$r_{n_k-n_k^{*(r)}}$ [g]	0 (1/hr)	–	$(D_x)_k$	1×10^{-3} (m^2/hr)	Equation (28)
$r_{n_1-n_1^{*(i)}}$ [h]	0.229 (1/hr)	–	$(d_p)_1$	850×10^{-9} (m)	–
$r_{n_k^{*(r)}-n_k}$	0 (1/hr)	–	$r_{n-n^{*(r)}}$	0.0227 (1/hr)	*Equation* (24)
$r_{n-n^{*(i)}}$ [i]	0.229 (1/hr)	–	$r_{n_1-n_1^{*(r)}}$	0.0227 (1/hr)	*Equation* (24)
Common physicochemical parameters			**Common physicochemical parameters**		
k_B [j]	1.78×10^{-16} (kg $m^2/(hr^2K)$)	(Weast, 1984)	L_x	0.6 (m)	–
A_{123} [k]	9.72×10^{-14} (kg m^2/hr^2)	(Murray & Parks, 1978)	α [r]	0.0048 (–)	(Syngouna & Chrysikopoulos, 2012)
A_{121} [l]	9.72×10^{-14} (kg m^2/hr^2)	–	g [s]	1.271×10^{8} (m/hr^2)	–
d_c	6×10^{-4} (m)	–	θ	0.42 (-)	(Syngouna & Chrysikopoulos, 2012)
ρ_w [m]	999.7(kg/m^3)	–	**DLVO**		
μ_w [n]	3.2 (kg/(m hr))	–	I_s [t]	0.1 (mol/m^3)	(Chrysikopoulos & Syngouna, 2012)
T [o]	298 (K)	–	N_A [u]	6.022×10^{23} (1/mol)	(Weast, 1984)
A_c	4.91×10^{-4} (m^2)	–	e [v]	1.602×10^{-19} (C)	(Weast, 1984)
ζ	0.637 (-)	(Feder, 1988)	ε_0 [w]	8.854×10^{-12} (C^2/(J m))	(Weast, 1984)
D_F	2.1 (-)	(Lin et al., 1989)	ε_r [x]	78.4 (-)	(Weast, 1984)
ρ_n [p]	1420 (kg/m^3)	–	Ψ_{p1} [y]	8.7 (mv) [d_1=850 nm]	–
ρ_b [q]	1610 (kg/m^3)	–	σ_{Born} [z]	5×10^{-10} (m)	(Ruckenstein & Prieve, 1976)

[a] $(D_x)_k$ [L^2/t] is longitudinal hydrodynamic dispersion coefficient of suspended nanoparticles that belong to cluster k.

[b] n_1^0 [np_k] is the initial constant aqueous phase concentration of first cluster, used in (12).

[c] $r_{n_1-n_1^{*(r)}}$ [1/t] rate coefficient of reversible nanoparticle attachment onto the solid matrix, of first cluster k=1.

[d] $r_{n_k-n_k^{*(i)}}$ [1/t] rate coefficient of irreversible nanoparticle attachment onto the solid matrix, that belong to cluster k.

[e] $r_{n_k^{*(r)}-n_k}$ [1/t] rate coefficient of reversible nanoparticle detachment from the solid matrix, that belong to cluster k.

[f] $r_{n-n^{*(r)}}$ [1/t] rate coefficient of reversible nanoparticle attachment onto the solid matrix used by the KC model.

[g] $r_{n_k-n_k^{*(r)}}$ [1/t] rate coefficient of reversible nanoparticle attachment onto the solid matrix, that belong to cluster k.

[h] $r_{n_1-n_1^{*(i)}}$ [1/t] rate coefficient of irreversible nanoparticle attachment onto the solid matrix, of first cluster k=1.

[i] $r_{n-n^{*(i)}}$ [1/t] rate coefficient of irreversible nanoparticle attachment onto the solid matrix used by the KC model.

[j] k_B [$M\cdot L^2/(t^2\cdot T)$] Boltzmann constant), used in (21).
[k] A_{123} [ML^2/t^2] Complex Hamaker constant (nanoparticle-water-collector), used in (23).
[l] A_{121} [ML^2/t^2] Complex Hamaker constant (nanoparticle-water-nanoparticle), used in (23).
[m] ρ_w [M/L^3] water density, used in (26)
[n] μ_w [$M/(L\cdot t)$] absolute water viscosity, used in (26)
[o] T [K] Temperature, used in (21).
[p] ρ_n [M/L^3] nanoparticle density, used in (26)
[q] ρ_b [M/L^3] bulk density of the solid matrix, used in (26)
[r] α [-] collision efficiency, used in (26).
[s] g [m/hr^2] acceleration of gravity, used in (26).
[t] I_s [mol/L] ionic strength, used in (23).
[u] N_A [1/mol] Avogadro's number, used in (23).
[v] e [C] elementary charge, used in (23).
[w] ε_0 [$C^2/(J\cdot L)$] permittivity of free space, used in (23).
[x] ε_r [-] relative dielectric constant of the suspending liquid, used in (23).
[y] Ψ_{p1} [mV] surface potential of a particle, used in (23).
[z] σ_{Born} [L] Born collision parameter, used in (23).

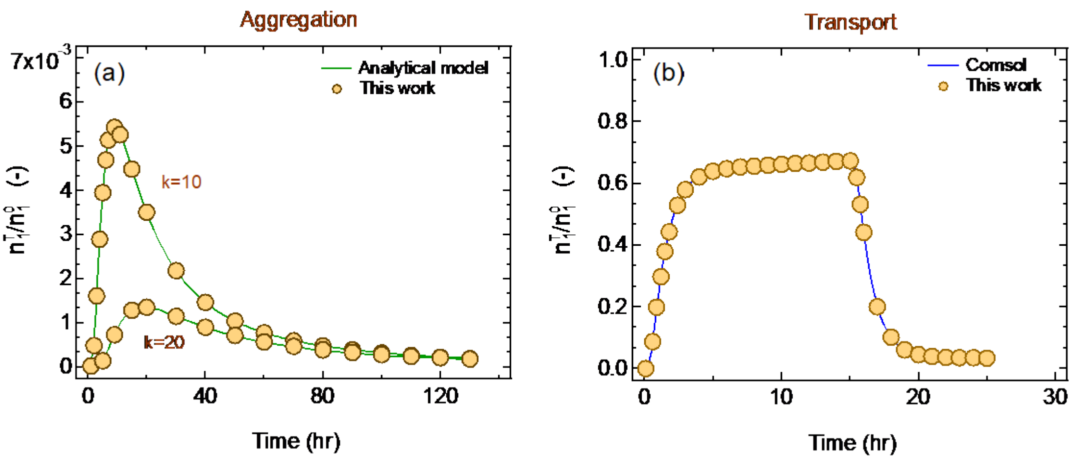

Figure 1. Dimensionless total number concentrations (n_1^T / n_1^0) as a function of time for nanoparticle: (a) aggregation based on analytical and numerical solutions for simple kernel k_{ij}=1 and two different clusters (k=10 and 20), and (b) transport based on the commercial software Comsol^{TM} and the present numerical model at x=0.6 m.

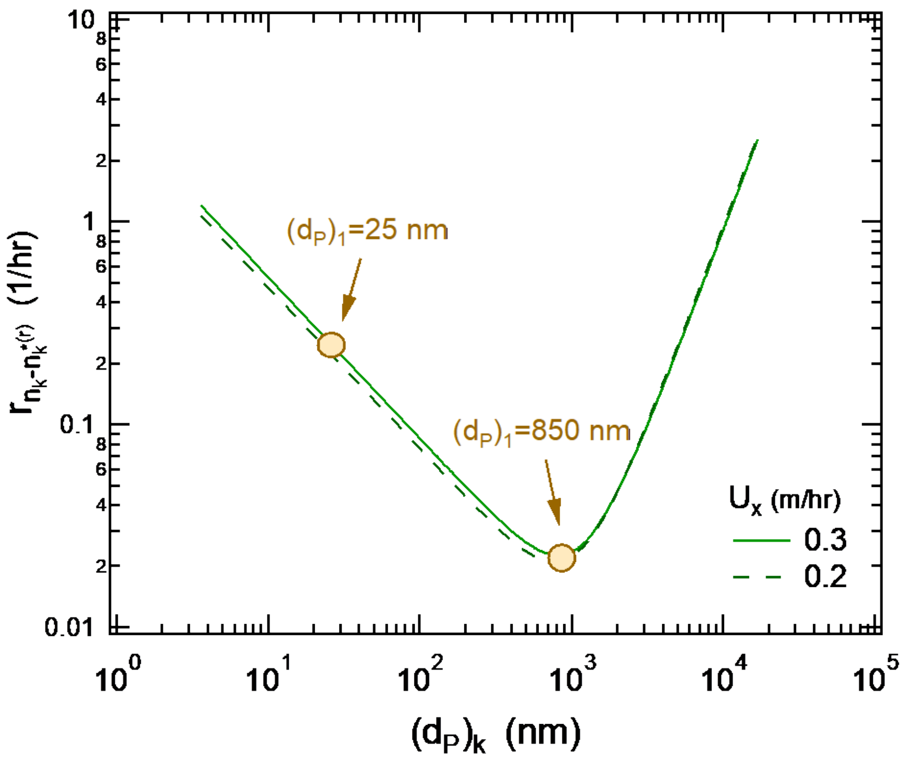

Figure 2. Forward attachment rate as a function of particle diameter, for two different interstitial velocities. The two aggregate diameters (d_{P1}) used in this study are shown.

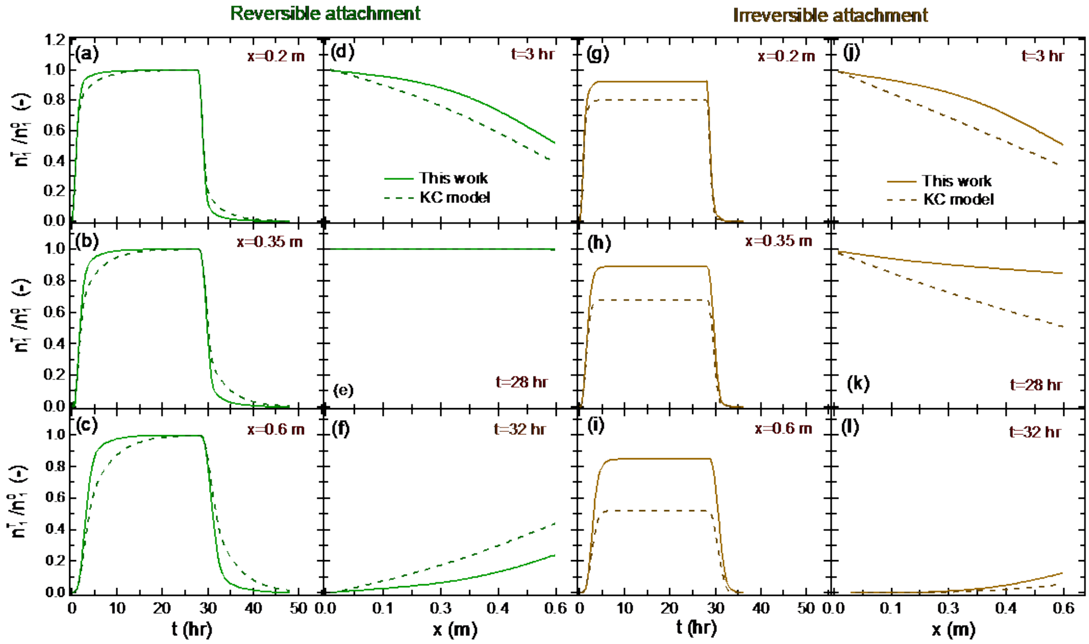

Figure 3. Dimensionless nanoparticle total number concentrations of cluster k=1, for both cases of reversible attachment and irreversible attachment, for a source of nanoparticles in the form of a broad pulse with t_p=28 hr, as a function of time at three different locations: (a)&(g) x=0.2 m, (b)&(h) x=0.35 m and (c)&(i) x=0.6 m, and a function of space for three different times: (d)&(j) t=3 hr, (e)&(k) t=t_p=28 hr, and (f)&(l) t=32 hr. The continuous curves are simulated by the present nanoparticle transport model and the dashed curves by the KC model.

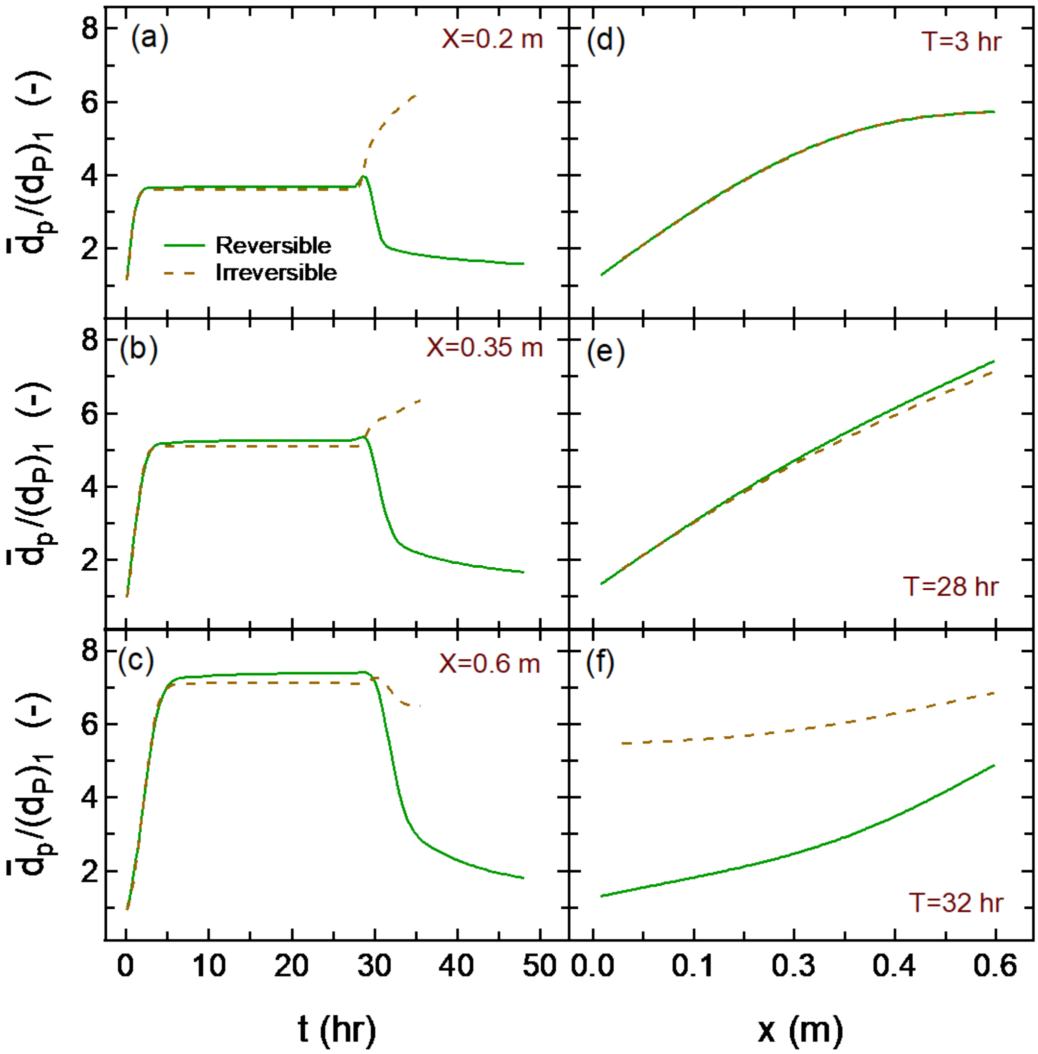

Figure 4. Dimensionless average size of suspended aggregates, for both cases of reversible attachment (solid curves) and irreversible attachment (dashed curves), for a source of nanoparticles in the form of a broad pulse with t_p=28 hr, as a function of time at three different locations: (a) x=0.2 m, (b) x=0.35 m and (c) x=0.6 m, and a function of space for three different times: (d) t=3 hr, (e) t=t_p=28 hr, and (f) t=32 hr.

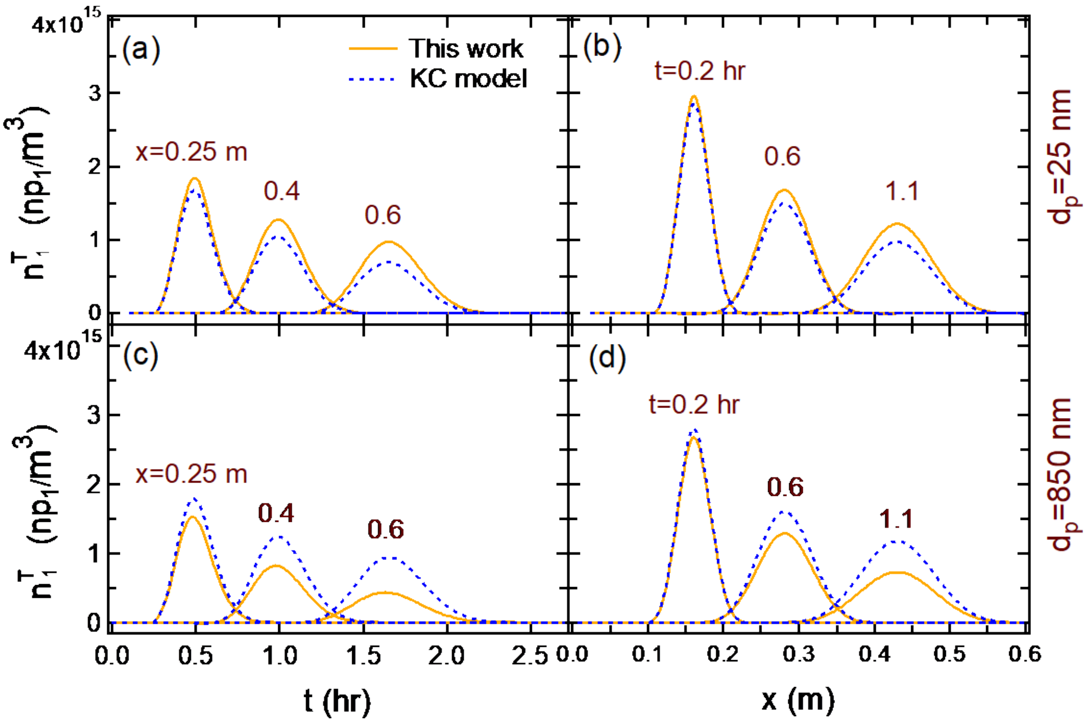

Figure 5. Total number concentrations of suspended nanoparticles of cluster k=1, introduced instantaneously in the 1-D aquifer, as a function of: (a)&(c) time at three different locations (x=0.25, 0.4, and 0.6 m), and (b)&(d) space at three different times (t=0.2, 0.6, and 1.1 hr). Two different nanoparticle sizes are considered ($(d_p)_1$ =25 and 850 nm). The continuous curves are simulated by the present nanoparticle transport model and the dashed curves by the KC model.

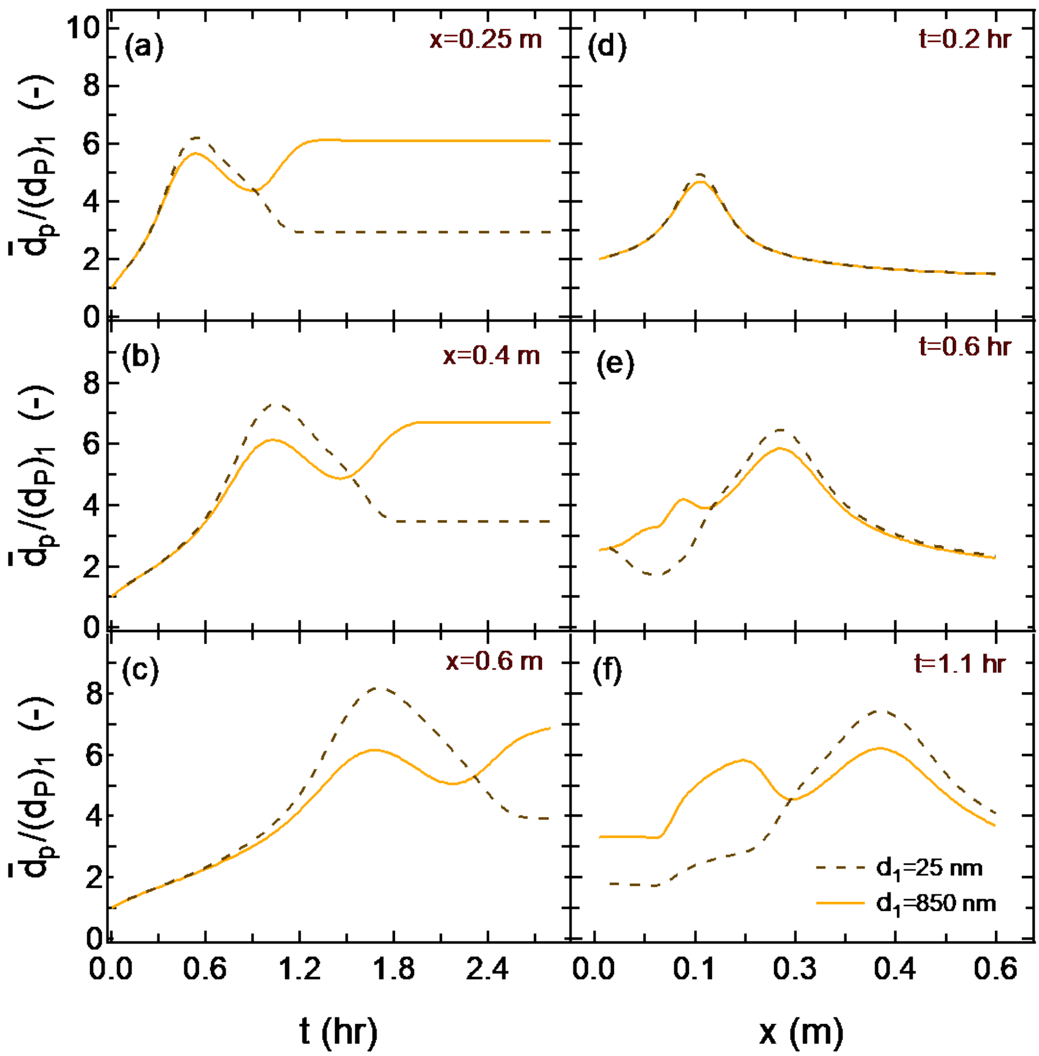

Figure 6. Dimensionless average size of suspended aggregates of nanoparticles introduced instantaneously in the 1-D aquifer, undergoing reversible attachment, simulated by the present nanoparticle transport model, as a function of time at three different locations: (a) x=0.25 m, (b) x=0.4 m and (c) x=0.6 m, and a function of space for three different times: (d) t=0.2 hr, (e) t= 0.6 hr, and (f) t=1.1 hr. The dashed curves corespond to nanoparticles with diameters $(d_p)_1 = 25$ nm, and the continuous curves corespond to nanoparticles with diameters $(d_p)_1 = 850$ nm.

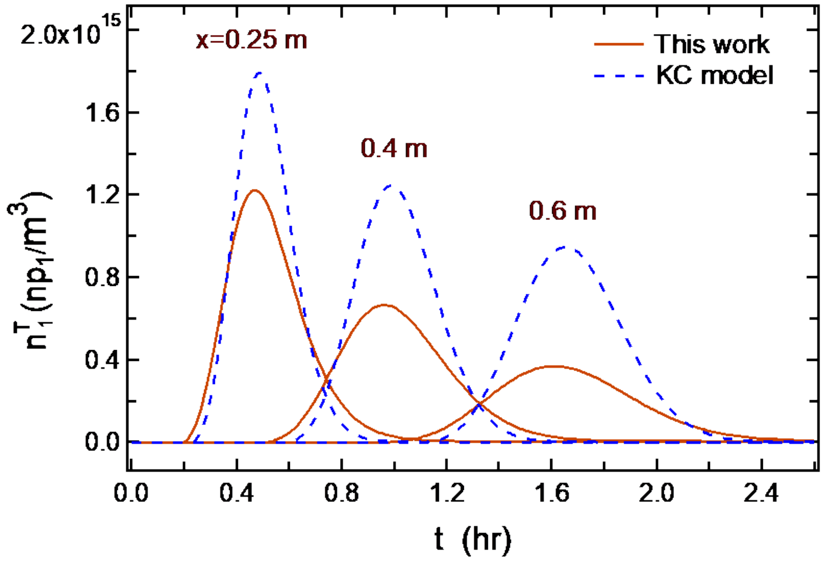

Figure 7. Breakthrough curves, at three different locations (x=0.25, 0.4, and 0.6 m), of total number concentrations of suspended nanoparticles of cluster k=1, for nanoparticles with $(d_p)_1$ =850 nm, introduced instantaneously in the 1-D aquifer. The continuous curves are simulated by the present nanoparticle transport model accounting for size-dependent dispersivity, and the dashed curves by the KC model with an invariant dispersion coefficient.

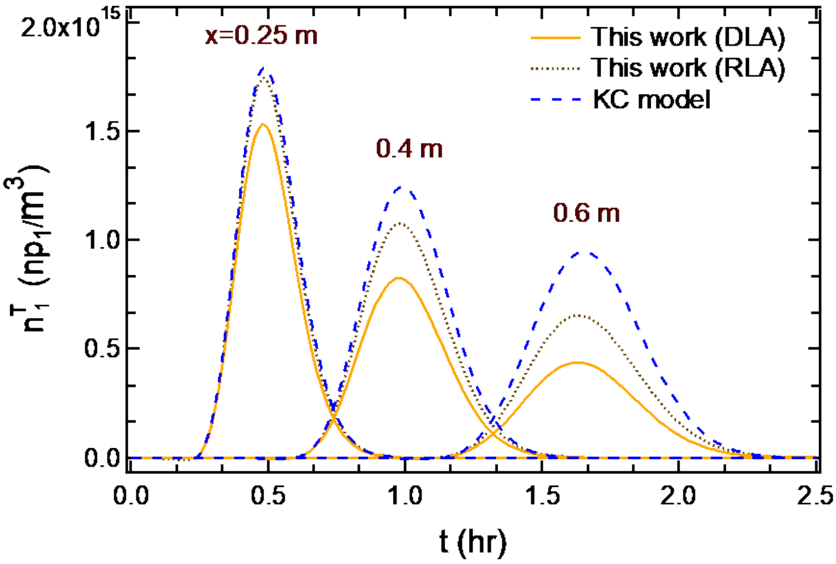

Figure 8. Breakthrough curves, at three different locations (x=0.25, 0.4, and 0.6 m), of total number concentrations of suspended nanoparticles of cluster k=1, for nanoparticles with $(d_p)_1$ =850 nm, introduced instantaneously in the 1-D aquifer. The continuous curves are simulated by the present nanoparticle transport model assuming diffusion-limited aggregation (DLA), the dotted curves by the present nanoparticle transport model assuming reaction-limited aggregation (RLA with Ψ_{p1}=8.7 [mV]), and the dashed curves by the KC model.

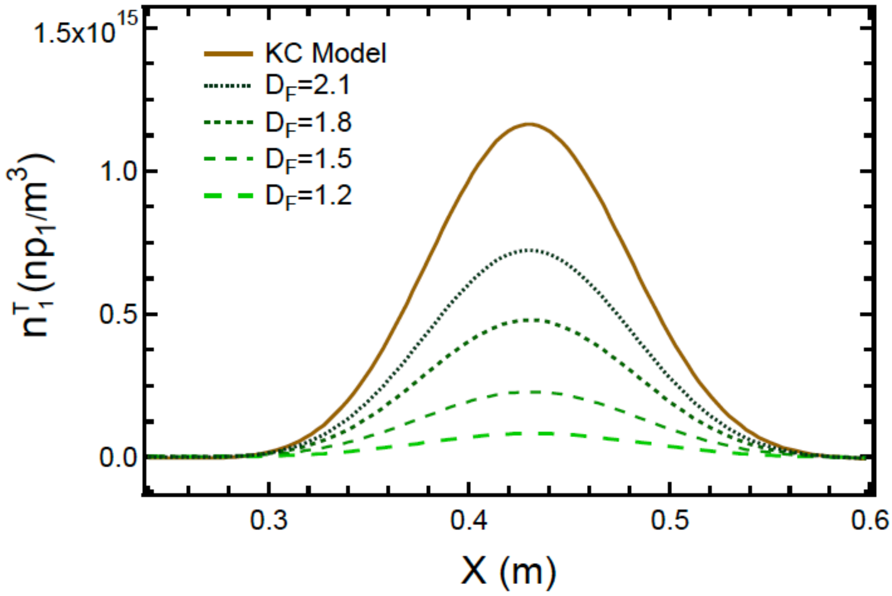

Figure 9. Total number concentrations of suspended nanoparticles of cluster k=1, introduced instantaneously in the 1-D aquifer, as a function of space at time t=1.1 hr, for several D_F [-] values. The continuous curve is simulated by the KC model, whereas all other curves are simulated by the present nanoparticle transport model. Initial nanoparticle size was $(d_P)_1 = 850$ nm.